Bachelor Thesis Physics and Astronomy

# Measuring the energy spectrum of tin ions from a laser produced plasma in a single shot.

*By:*

**Robin van Straaten.**

*Conducted between 26 May 2025, and 10 July 2025.*

| | |
|---|---|
| *Student number:* | 14590956 |
| *Research institute:* | ARCNL |
| *Research group:* | EUV Plasma Processes |
| *Daily Supervisor:* | Laurens van Buuren |
| *Assessor* | Oscar Versolato |
| *Examiner:* | John Sheil |

# Contents

# 1 Introduction

In 1965, Gordon Moore noticed great improvements in the microchip industry and came up with what is now known as Moore's law: the number of transistors on microchips doubles every two years. This law still holds since the need for smaller and more efficient chips continues to grow for applications such as smartphones, financial market infrastructure, and the development and widespread use of artificial intelligence.

Currently, the most advanced chips are made by ASML machines, which according to CNBC has the chip-making market under its control [1]. These machines use extreme ultra-violet (EUV) light with a wavelength around 13.5 nm to etch the images on the chip in a process called nanolithography. This 13.5 nm light is made by a laser produced plasma (LPP). This LPP is made by shooting a high-power laser onto a tin droplet, creating an ion explosion. In this ion explosion, ions with different charges are moving in all directions. The amount of ions, together with their kinetic energy and charge is essential information to, for example, prevent these ions from damaging the mirrors and other equipment in the chip making machine.

Currently, Faraday cups with a retarding field analyzer (RFA) are used at ARCNL to measure the amount of ions and their kinetic energy. While this is a way to accurately measure the energy spectrum of different ionization states, it cannot be done in a single shot and requires different settings, the retarding field, which takes a long time [2]. Single-shot measurements can also be used to measure the spectrum of individual tin droplets without having to average out the measurements. Therefore when working with flying tin droplets and ion explosions, the Thomson Parabola would be preferred.

The Thomson Parabola is another way of measuring the energy spectrum of ions coming out of an LPP. Using a parallel magnetic and electric field, the ions from the LPP are separated by mass, speed and charge. If the ions have the same mass, the magnetic and electric field will separate them by charge resulting in a parabola shaped line per charge [3]. The further the ion is up the parabola, the lower its kinetic energy.

This method in principle is able to do single shot measurements, additionally making the measurements take significantly less time compared to the RFAs. The problem is that the accuracy in comparison with a Faraday cup is unknown and would depend on the experimental setup. It also takes up more space than a Faraday cup.

This thesis aims to answer the question: How to measure the energy spectra of ions coming out of an LPP with a Thomson Parabola, focusing on the theory and data analysis needed to do a measurement and discussing the accuracy and implications. The work done in this thesis is meant to be further worked upon. Therefore the steps taken in the code of the data analysis and the derivation of the formulas used will be explained in their entirety.

## 2 Theory

In this section the main point of discussion is going to be how far the ions are deflected due to the magnetic and electric field when the ions reach the detector. In a previous report by Lennart Tinge [4] about the Thomson Parabola the setup in figure 1 was used. The ions from the LPP pass through two apertures before entering the magnetic and electric fields. These fields deflect the ions and using eq. 1 and eq. 2 the kinetic energy was calculated.

$$x = \frac{qBL_B}{\sqrt{2mE_{\text{kin}}}}(\frac{1}{2}L_B + l_B) \tag{1}$$

$$y = \frac{qEL_E}{2E_{\text{kin}}}(\frac{1}{2}L_E + l_E), \tag{2}$$

Here $x$ and $y$ are the displacement length of the ions in their respective directions, $q$ the charge of the ion, $B$ the magnetic field, $E$ the electric field, $m$ the mass of the ion, $E_{\text{kin}}$ the kinetic energy, $L_E$ and $L_B$ the length of their respective fields in the $z$-direction and $l_E$ and $l_B$ the length from the fields to the detector. The reason we call this a parabola, is because when the kinetic energy of these two formulas gets equated to each other, the formula for $y$ has an $x$ component.

The limitations of this formula are that it assumes that the electric and magnetic fields are homogeneous, like in figure 1. Furthermore it assumes that the speed of the ions is not slowed down due to the magnetic field. This assumption can be examined by deriving the extent to which the ions slow down in the $z$-direction due to the magnetic field, while still assuming the fields are homogeneous. Deriving or examining the extent to which the fields are not homogeneous is outside of the scope of this thesis, but is explored in Tinge's internship report [4].

### 2.1 Derivation of the deflection

In the setup described in figure 1, the tin ions go through two apertures in the $z$-direction and then pass the magnetic field and electric field which are both in the y-direction.

#### 2.1.1 Deriving the x-deflection

To calculate the deflections of the ions by the magnetic field, we use Coulombs formula:

$$\vec{F}_B = q\vec{v} \times \vec{B}. \tag{3}$$

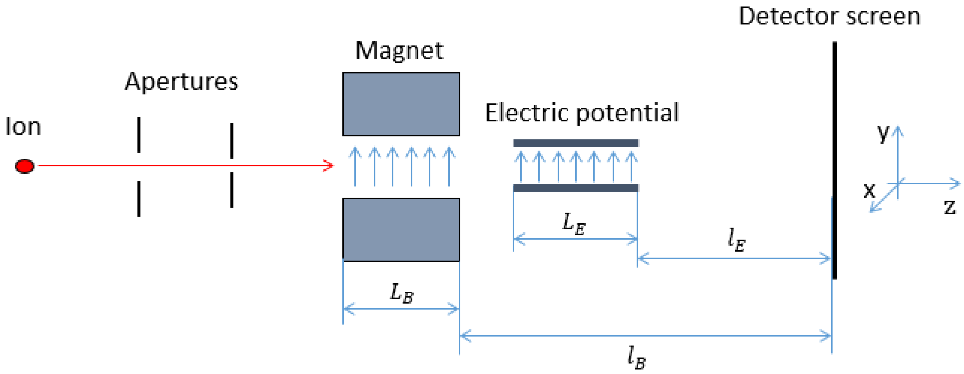


Figure 1: Experimental setup to help visualize the constants used in the equations. The ions move in the $z$-direction and first pass two apertures, then a magnet and an electric potential and finally reaching the detector. $l_B$ and $l_E$ are the width of their respective fields and $L_B$ and $L_E$ are the length between the end of their field to the detector, which is imagined as a two dimensional line.

With a magnetic field only pointing in the $y$ direction, the cross product becomes:

$$\vec{F}_B = -qv_zB_y\hat{x} + qv_xB_y\hat{z}. \tag{4}$$

From this we can isolate the x-component and equate it to mass times acceleration in the x-direction. Doing this for both the $x$ and the z directions, we get

$$\dot{v}_z = \frac{qB_y}{m}v_x = \omega v_x \tag{5}$$

and

$$\dot{v}_x = -\frac{qB_y}{m}v_z = -\omega v_z \tag{6}$$

where $\omega$ is the cyclotron frequency, also known as the Larmor frequency. Using the start conditions $v_z(0) = v_0$ and $v_x(0) = 0$, we know that the solution of the differential equation is

$$v_z(t) = v_0\cos(\omega t), \tag{7}$$

$$v_x(t) = -v_0\sin(\omega t). \tag{8}$$

Using these formulas for speed, we can calculate the distance the ions are deflected. We will do this in two phases, the first in which the ions are still in the magnetic field, and the second in which they have left the fields and are not acted upon by a force. The ions travel the length of the magnetic field, $L_B$, in the $z$-direction. We know from eq 4 that once the ions are accelerated in the x-direction, they will also decelerate in the $z$-direction, making the time they spend in the field, $t_1$, longer. To calculate $t_1$, we will calculate the distance in $z$-direction of the field using $v_z$

$$z(t_1) - z(t=0) = L_B - 0 = \int_0^{t_1} v_z(t)dt = \int_0^{t_1} v_0\cos(\omega t)dt = \frac{v_0}{\omega}\sin(\omega t_1), \tag{9}$$

so with $L_B = \frac{v_0}{\omega}\sin(\omega t_1)$,

$$t_1 = \frac{1}{\omega}\arcsin(\frac{\omega L_B}{v_0}). \tag{10}$$

Using eq 10, we can calculate the displacement of the ion when leaving the homogeneous magnetic field.

$$x(t_1) - x(0) = \int_0^{t_1} v_x(t)dt = \int_0^{t_1} -v_0\sin(\omega t) = \frac{v_0}{\omega}(\cos(\omega t_1) - 1). \tag{11}$$

For phase two, where we are calculating the displacement after the ions leave the fields. For this the speed of the ions moving in the $z$-direction, towards the detector, and the speed in the x-direction needs to be known.

$$v_z = v_0\cos(\omega t_1) \tag{12}$$

$$v_x(t_1) = -v_0\sin(\omega t_1) = -v_0\sin(\arcsin(\frac{\omega L_B}{v_0}) = -\omega L_B. \tag{13}$$

The time the ions travel from the end of the magnetic field to the detector is

$$t_2 = \frac{l_B}{v_z(t_1)} = \frac{l_B}{v_0\cos(\arcsin(\frac{\omega L_B}{v_0}))}. \tag{14}$$

Then, the displacement from the end of the field to the detector is:

$$x_2 = v_x(t_1)\cdot t_2 = -\frac{\omega L_B l_B}{v_0\cos(\arcsin(\frac{\omega L_B}{v_0}))}. \tag{15}$$

So, the total displacement by the magnetic field is the sum of $x_1$ and $x_2$.

$$x = x_1 + x_2 = -\frac{v_0}{\omega}(1 - \cos(\omega t_1)) - \frac{\omega L_B l_B}{v_0\cos(\omega t_1))}. \tag{16}$$

Note that the total x-displacement blows up in this formula when $\omega t_1 = \pi/2$. In this case the magnetic field is big enough, or the ion is moving slow enough, that the direction the ion can be deflected over 90°, making $v_z = 0$ and coincidentally making it unlikely for the ion to reach the detector.

To get $E_{\text{kin}}$ from this equation, which is needed for further analysis, $v_0$ and $t_1$ needs to be rewritten. Filling in $t_1$ in eq 16, using $\cos(A) = \sqrt{1 - \sin^2(A)}$ we get

$$\cos(\omega t_1) = \cos(\arcsin(\frac{\omega L_B}{v_0})) = \sqrt{1 - (\frac{\omega L_B}{v_0})^2} = \frac{\sqrt{v_0^2 - \omega^2 L_B^2}}{v_0} \tag{17}$$

(assuming $v_0 \geq 0$). Filling in the term $\omega$ because it has a mass term, this equation becomes:

$$\cos(\omega t_1) = \frac{\sqrt{m^2 v_0^2 - (qBL_B)^2}}{mv_0} = \sqrt{\frac{2mE_{\text{kin}} - (qBL_B)^2}{2mE_{\text{kin}}}}. \tag{18}$$

Here it is noteworthy that there is no solution when $2mE_{\text{kin}} \leq (qBL_B)^2$, or $p_{\text{ion}} \leq qBL_B$, where $p_{\text{ion}}$ is the impulse of the ion. This is for the same reason eq 16 can blow up, where with a big enough magnetic field the particles can deflect over 90° resulting in them not hitting the detector plate. This will be seen more clearly when we rewrite the $x$ function with this $\cos(\omega t_1)$ definition.

$$x = -\frac{\sqrt{2mE_{\text{kin}}}}{qB}(1 - \sqrt{\frac{2mE_{\text{kin}} - (qBL_B)^2}{2mE_{\text{kin}}}}) - \frac{qBL_b l_b}{\sqrt{2mE_{\text{kin}} - (qBL_B)^2}}, \tag{19}$$

$$x = -\frac{1}{qB}(\sqrt{2mE_{\text{kin}}} - \sqrt{2mE_{\text{kin}} - (qBL_B)^2}) - \frac{qBL_B l_B}{\sqrt{2mE_{\text{kin}} - (qBL_B)^2}}. \tag{20}$$

### 2.1.2 Deriving the y-deflection

The deflection in the y-direction is caused by a homogeneous electric field pointed in the y-direction. In this setup, the electric field is placed after the magnetic field. This coincidentally makes the derivation easier because for the x-deflection the $v_y$ does not have to be incorporated. The electric field is created using two plates parallel to each other connected to a voltage, making them capacitors. The formula for a homogeneous electric field between two capacitors is as follows:

$$\vec{E} = \frac{\sigma}{\epsilon_0}\hat{y} = \frac{Q}{A}\frac{1}{\epsilon_0}\hat{y} = \epsilon_0 \frac{V}{d}\frac{1}{\epsilon_0}\hat{y} = \frac{V}{d}\hat{y}. \tag{21}$$

Here, $V$ is the voltage put on the capacitors with $d$ being the distance between them. The other constants shown for derivative purposes are $\sigma$, the electric field potential, $\epsilon_0$, the permittivity of free space, $Q$, the total charge on a surface and $A$, which is the surface area. Using $\vec{F} = q\vec{E}$, this formula becomes:

$$\vec{F}_E = \frac{qV}{d}\hat{y}. \tag{22}$$

Now in phases again, we will get the y-deflection first during the acceleration process and then when the ion is not in an electric field. With the field being $L_E$ long, it will be in that field for $t_{1_y} = \frac{L_E}{v_z}$ seconds. Using the Newton second law of motion and the eq 22, we can calculate the acceleration:

$$\vec{F}_E = ma_y = \frac{qV}{d}\hat{y},$$

$$\vec{a} = \frac{qV}{dm}\hat{y}.$$

So,

$$y_1 = \frac{1}{2}at_{1_y}^2 = \frac{qV}{2dm}t_{1_y}^2 = \frac{qV}{2dm}\frac{L_E^2}{v_z^2(t_1)}, \tag{23}$$

and after the ion leaves the electric field it is accelerated to $v_y$ speed:

$$v_y = a_y t_{1_y} = \frac{qV}{dm}t_{1_y}\hat{y}. \tag{24}$$

where $t_{1_y}$ is the time the ion spends in the electric field. Using eq 24 to calculate phase two, we get:

$$y_2 = v_y t_{2_y} = \frac{qV}{dm}t_{1_y}t_{2_y} = \frac{qV}{dm}\frac{L_E}{v_z(t_1)}\frac{l_E}{v_z(t_1)}. \tag{25}$$

Adding $y_1$ and $y_2$ together, we get

$$y = y_1 + y_2 = \frac{qV}{2dm}\frac{L_E^2}{v_z(t_1)^2} + \frac{qV}{dm}\frac{L_E}{v_z(t_1)}\frac{l_E}{v_z(t_1)} = \frac{qVL_E}{2dmv_z(t_1)^2}(L_E + 2l_E), \tag{26}$$

with $y$ being the displacement of the ion when it hits the detector, $q$ the charge in Coulomb, $V$ the voltage, $d$ the length between the charged plated, $m$ the mass of the ion, $L_E$ the width in $\hat{z}$ of the homogeneous electric field/charged plates, $l_E$ the length from the end of the electric field to the detector and $v_z$ is the speed of the ion in the z direction. This speed is not the same as $v_0$ since it has been slowed down by the magnetic field, so $E_{\text{kin}}$ cannot be calculated by $v_z$ and eq 26 has to be rewritten using a combination of eq 7 and 18.

Using $E_{\text{kin}} = \frac{1}{2}mv_0^2$ we get $v_0 = \sqrt{\frac{2E_{\text{kin}}}{m}}$, meaning:

$$v_z(t_1) = v_0\cos(\omega t_1) = \sqrt{\frac{2E_{\text{kin}}}{m}}\sqrt{\frac{2mE_{\text{kin}} - (qBL_B)^2}{2mE_{\text{kin}}}} = \frac{\sqrt{2mE_{\text{kin}} - (qBL_B)^2}}{m}. \tag{27}$$

Filling this into eq 26, we get

$$y = \frac{qmVL_E}{d}\frac{(L_E + 2l_E)}{4mE_{\text{kin}} - 2(qBL_B)^2}. \tag{28}$$

The only difference between this formula and the one used in Tinge's report is that $E$ is filled in like $\frac{V}{d}$ and the change in speed in the $z$-direction by the magnetic field is taken into account.

## 2.2 Comparing the formulas

Though eq 1 and 2 are different from eq 20 and 28, when $2mE_{\text{kin}} \gg (qBL_B)^2$, eq 20 and 28 will approximately become the same function as eq 1 and 2. The formulas can be numerically analyzed to check when the differences between them are significant. Using typical values B=0.018 T, V=40 V, d=15 mm and the dimensions noted in figure 5, the formulas are plotted. Starting with the difference in equations 1 and 20, ranging from $E_{\text{kin}}$ = 0to 50 eV, in figure 2a and from 50 eV to 500 eV in figure 2b. These coordinate bounds are chosen so that the difference when significant is visible.

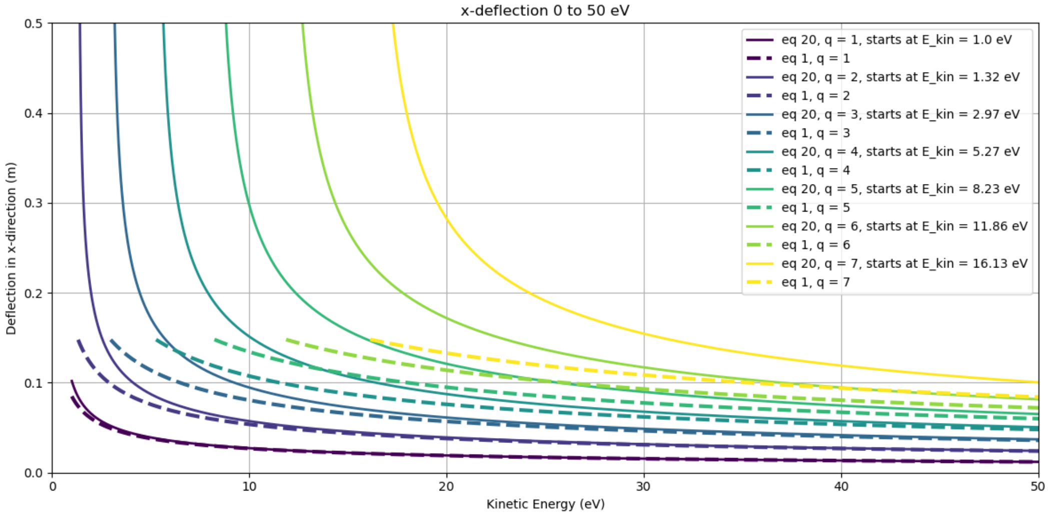


(a)

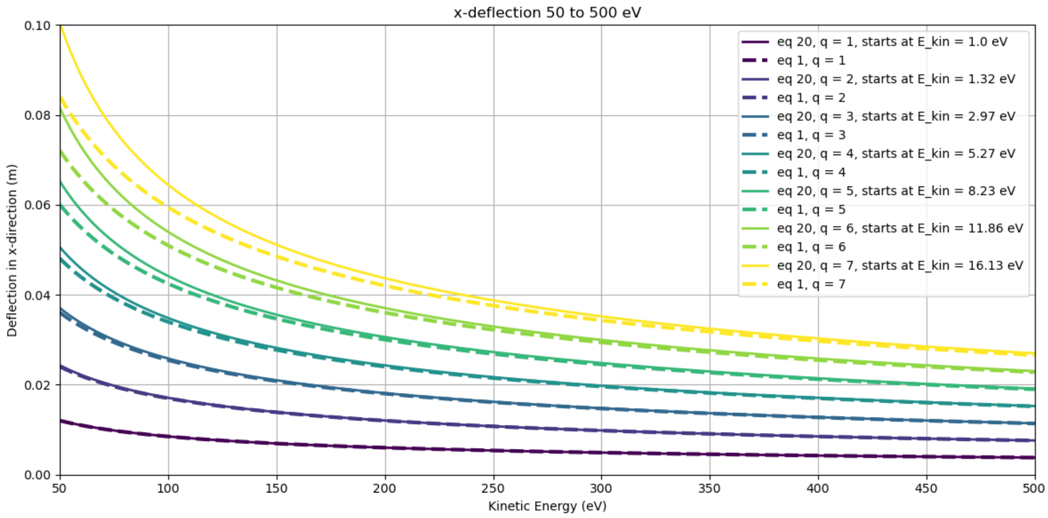


(b)

Figure 2: Comparison between eq 1 and 20 for tin ions with a charge 1+ up to 7+ with typical experimental constants, illustrated in figure 5. There is a significant difference at energies from 0 eV to around 200 eV depending on the charge. The starting points are numerically determined with two decimal accuracy according to $2mE_{\text{kin}} \leq (qBL_B)^2$.

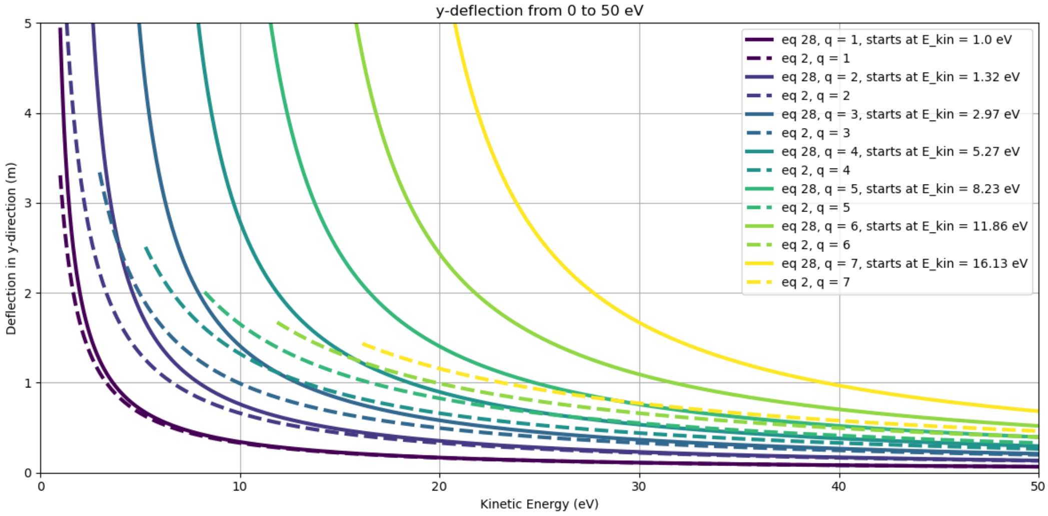


(a)

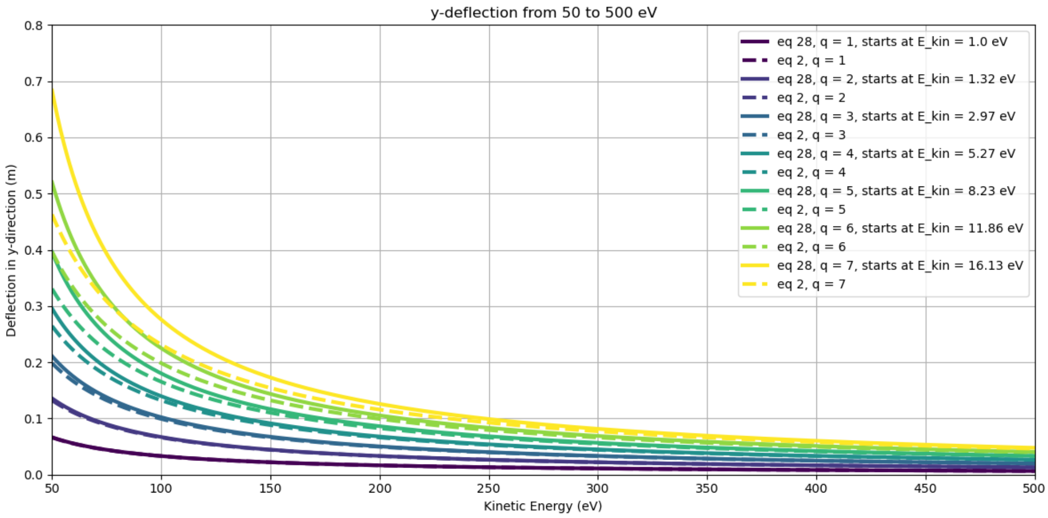


(b)

Figure 3: Comparison between eq 2 and 28 for tin ions with a charge 1+ up to 7+ with the constants mentioned in figure 5. There is a significant difference at energies from 0 eV up to around 150 eV depending on the charge. The starting points are numerically determined with two decimal accuracy according to $2mE_{\text{kin}} \leq (qBL_B)^2$.

In figure 2a and 3a there is a difference in deflection, especially when the kinetic energy is low. The starting points, determined when in steps of 0.01 eV, are where $2mE_{\text{kin}} \leq (qBL_B)^2$ is valid for the first time. When looking at the higher energies, the difference seems to be lower for the y-deflection. There is however a difference visible between the equations for energies lower than 150 eV.

To indicate the significance of this difference, figure 4 shows eq 1 and 2 as a thin line alongside eq 20 and 28, which were plotted as a rainbow plot. The values filled into the formulas are taken from the experimental setup, see figure 5, with a magnetic field strength of 18 mT and a voltage of 40 V on the capacitor plates, which is around the expected order of strength for both fields. Figure 4 shows that there is no significant difference between the formulas derived in this section and Tinge's formulas when looking at the expected scale of the experiment.

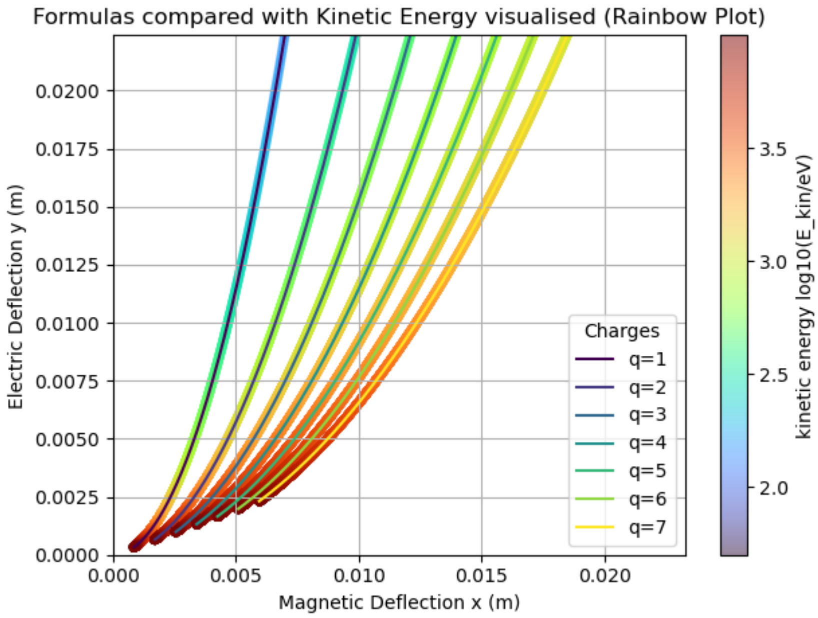


Figure 4: Formulas 1 and 2, plotted as thin lines, compared with eq. 20 and eq. 28, plotted as a rainbow plot, at the scale of the typical deflection.

## 3 Method

In short, in our Thomson Parabola ions are coming from a laser induced plasma explosion, going through two apertures entering the Thomson Parabola. Here they go through a magnetic and electric field. The magnetic field, generated by an electric current through a coil, is not known but the electric field is determined from the set potential. After passing through these fields the non-charged particles get blocked while the other hit the detector, see figure 5 for a schematic overview of the setup and dimensions filled in. With the data from the detector, the magnetic field is fitted as an unconstrained variable. Furthermore, the counts along the parabola are summed in bins to make a first version of a energy spectrum. The specifics of the setup and steps taken in the data analysis are listed in the sections below.

## 3.1 Setup

In a vacuum chamber with a pressure of $8 \times 10^{-6}$ mbar during the experiment a plasma explosion is made by a diode-pumped Nd:YAG laser, specifically the Surelite I-10 laser. The beam of the Surelite I-10 laser has a wavelength of 1064 nm and a beam width of 6 mm. It is pulsed at 10 Hz laser that shoots 10 times for 4 ns to 7 ns every second perpendicularly onto a sheet of tin. This sheet of tin is moved a little after every 15 shots to not make the laser burn through the sheet.

At a 30° angle to the left from the sheet the ions go through two apertures. The first aperture has a diameter of 100 µm and the second has a diameter of 550 µm. These apertures filter out unwanted debris, allowing an ion beam with a diameter small enough for the eventual data to be analyzed accurately to pass through. After exciting the apertures the ions enter the magnetic field. The magnetic field is created by a coil of which the amount of windings is unknown, but the current put on the coils is 40 mA. This coils has a yoke that guides the field around a rectangular vacuum tube, ensuring the magnetic has the desired field lines. The width of the magnetic field, meaning the distance the ions travel through the magnetic field, is 50 mm. After leaving the magnetic field, the ions enter the electric field, created by two capacitor plates with a potential difference of 40 V divided between the two plates. This is done so that the potential in the middle of the two plates is 0 V, avoiding a slowing down of the ions caused by a potential difference.

After the fields, the neutral tin and light emitted from the plasma are stopped by the beam stopper, while the ions hit the detector. The detector is a two channel microchannel plate detector (MCP), specifically MCP-75-2-40-P43-CF160, which has a diameter of 77 mm, a channel diameter/pitch of $21\mu m/26.5\mu m$, an aspect ratio of 40 : 1 and a gain of $1 \cdot 10^6$e/e. What these specifications mean is that ions that hit the MCP enter the channels where they create a cloud of electrons. This electron cloud hits a phosphor plate, inducing fluorescence, of which a picture is taken. Per measurement, 5 to 10 pictures are taken, with one picture for each shot. While this setup can analyze single-shot measurements, to prevent individual anomalies, the average of a couple of pictures is taken. The images corresponding to each measurement are opened in Python and the values are averaged over the amount of shots.

## 3.2 Data analysis

### 3.2.1 Rotating the image

To fit the parabolas on these images, the origin, where the neutral particles would hit the detector, and directions of the $x$ and y-axis needs to be known. These directions are de-

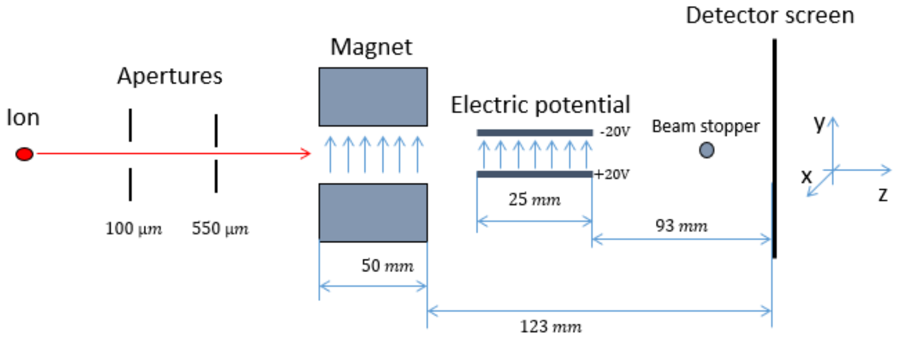


Figure 5: Experimental setup with dimensions filled in

termined by fitting a straight line through a measurement where only one field is on. For the measurement where only the electric field is on, the image is averaged over measurements with different field strength applied. So the measurements done for the electric field only image is one with 60 V, 80 V, 100 V, 120 V, and 160 V. Up to 100 V the laser intensity was 30 mJ. For the 120 V and 160 V measurements the laser intensity was 60 and 260 mJ respectively. Then this averaged data is masked and a line is fitted on this data, using the following formula:

$$y = ax + b. \tag{29}$$

For the measurement with only the magnetic field on, there was no need to stack multiple images with different magnetic field strengths because the line from the measurement with 1200 mA on the coils and 30 mJ laser was already over a long and straight enough range to fit over.

With the result of both fits we can determine the point of intersection, which will be the point of origin. Then the magnetic field fit is rotated to the x-axis and the data from only the electric field on is examined on how well it overlaps with the y-axis. After the picture is rotated, the values from a zero-measurement, where there is no electric or magnetic field but an equally intense laser, is subtracted from the measurements. This measurement is also averaged like the others.

### 3.2.2 Masking the data

The data is masked so that each parabola can be individually analyzed. With these individual parabolas, an upper and lower end magnetic field strength is defined. The upper bound is where the parabola is slightly steeper than the data, while the lower bound is less steep and has 20 pixels offset in the negative y-direction. The bounds are determined by hand, ensuring that no data is outside of the bounds. Then the full dataset is shown with masks applied for all visible charge state is shown to indicate the masks used. Additionally, the first charged state with a rainbow plot on the upper and lower bound of the mask is shown to indicate the range of energies in specific regions in the first charged state.

### 3.2.3 Fitting and creating a count energy spectrum

To fit the data, a weighted average of the distance between the fitted line and each pixel in the $q = 1$ masked dataset is made, where the intensity on the pixel is the weight. This weighted average is referred to as the cost in this analysis and is calculated with this equation:

$$\text{cost} = \frac{\sum_i^N w_i \cdot d_i}{\sum_i^N w_i}, \tag{30}$$

where $N$ is the total number of pixels, $w_i$ the intensity of pixel $i$ and $d_i$ the distance from pixel $i$ to the fitted line. Note that pixels without weight, intensity = 0, are not counted in this average.

This cost is minimized using the minimize function from Scipy's optimize package, with the Nelder-Mead method [5], the cost is minimized. The line fitted with the lowest cost is the best fit. To make sure the fit runs correctly, the cost of 200 linear spaced magnetic field strengths between 0.018 and 0.0322 T is calculated and plotted. Then the best fits are compared on the first charge state data, then on the unmasked data.

After examining the fit, all the charge states visible in the data are individually examined as described by section 3.2.2. On the upper bound parabola points, spaced apart by a log-scale in kinetic energy, are plotted using eq 20 and 28. The values of the pixels closest to these points are summed onto that point, making each plotted point a bin for a kinetic energy spectrum.

## 4 Results

The results are presented in the same order as the method. Starting with the measurements and fits to find the origin and the needed rotation of the image. Then showing the masks put on the data, the fit over the first charged state plus its cost values and finally showing the energy spectrum.

### 4.1 Rotating the image results

Figure 6 shows the data from only the E-fields on and the B-field on, and masking them accordingly.

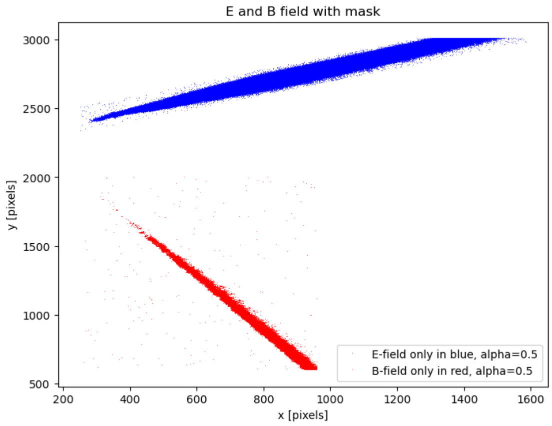


Figure 6: In red the data from the measurement of only the magnetic field on with a laser intensity of 30 mJ and a magnetic field strength of 1200 mA, visualized in red. In blue the measurements with electric fields at 60 V, 80 V, 100 V with 30 mJ, 120 V with 60 mJ, and 160 V with 260 mJ averaged over one image. This averaging out was needed to make the fit more accurate. It also makes the fit usable for wider ranges of electric fields.

Performing the fit with eq 29 on the electric field data, we get $a = 0.51279(35)$ and $b = 2273.21(34)$. The fit can be seen in figure 7 together with the mask put on the electric fields.

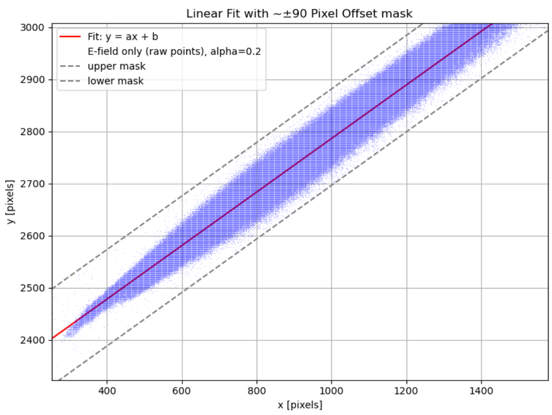


Figure 7: Electric fields from measurements 60 V, 80 V, 100 V with 30 mJ, 120 V with 60 mJ, and 160 V with 260 mJ averaged out, masked and fitted with eq 29. The result of the fit is $a = 0.51279(35)$ and $b = 2273.21(34)$

Performing the same fit on the data where only the magnetic field was on, we get $a =$

−1.9337(25) and $b = 2437.9(1.9)$. Using these results, the intersection was calculated to be $x = 67.33(78)$ and $y = 2307.74(53)$ pixels in the figure. Additionally, the angle between the lines is 89.803(46)°. In figure 8 both the fits and the point of intersection with coordinates are visible in a figure where the $x$ and y-axis has the same scaling.

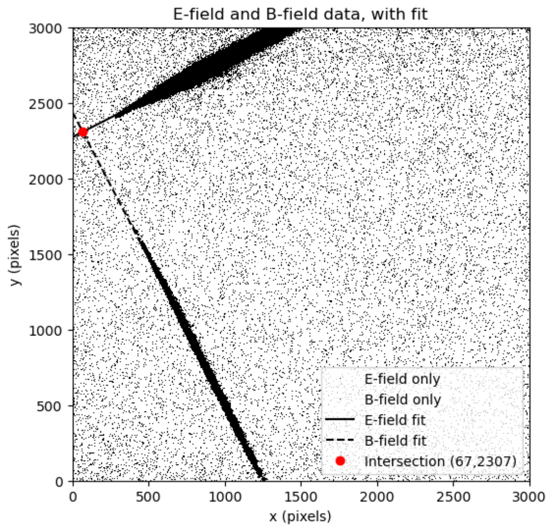


Figure 8: The unmasked data from both the measurements where only one field, electric or magnetic, is turned on. Here also the fit done on the masked data of figure 6 is plotted along with their point of intersection, which is the point of origin in this setup.

Using the most accurately defined slope, which is from the magnetic field, the angle between the slope and the x-axis is calculated to be −62.654(30)°. In figure 9 the same masked data with only the electric field on as in figure 6 is plotted when rotated as much as the angle previously described and being offset to make the intersection point the point of origin. This shows how the data overlaps with the y-axis.

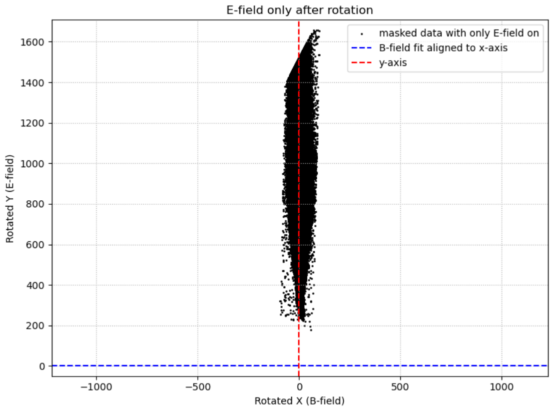


Figure 9: The masked data from the measurements where only the electric field was on angled by the same angle between the magnetic field fit and the x-axis, seen as the blue dashed line. The y-axis is plotted as the red dashed line to make comparing it with the data easier.

From here on, all the figures with data the same rotation and offset like figure 9 is applied. Like in figure 10a, where no mask is put on the image and only the zero measurement is subtracted. Figure 10b shows the same figure but with contrast where the pixel intensity is between 10 and 100, instead of 0 and 255

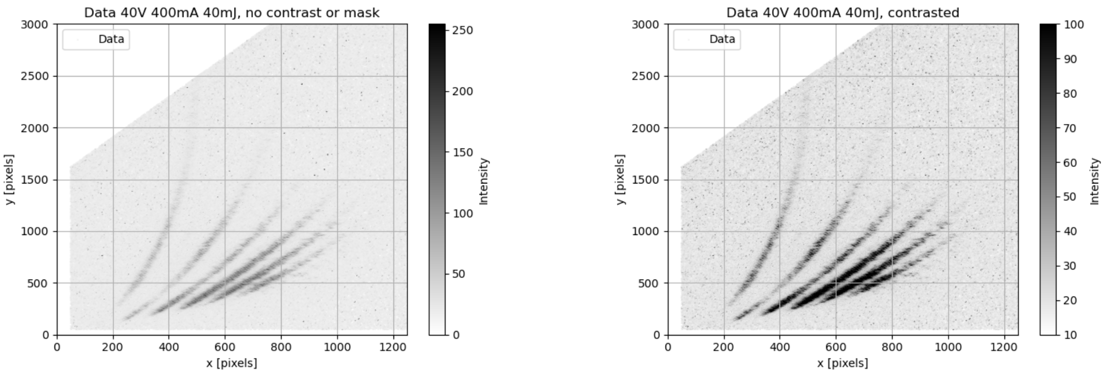


(a)

(b)

Figure 10: Same data of the measurement with 40 V, 400 mA and 40 mJ, but 10a has no contrast applied while 10b does. Both figures have the zero measurement with 40 mJ laser subtracted.

## 4.2 Masking the parabolas

The masks on the parabolas on the measurement with 40 V, 400 mA and a 40 mJ laser, with the same contrast as 10b, is shown in figure 11

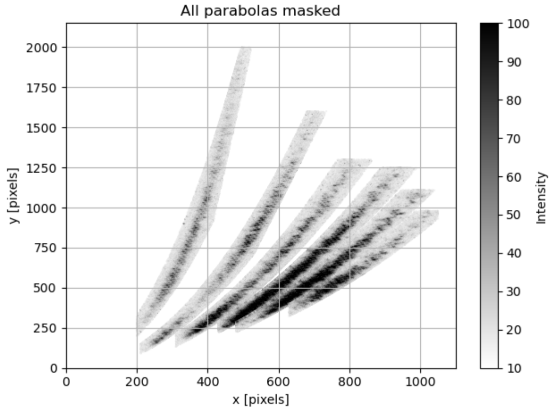


Figure 11: Masked parabolas of measurement 40 V, 400 mA and 40 mJ. The masks are made by only allowing values withing a lower and upper bound of eq. 20 and eq. 28, as well as only allowing values lower or higher then a certain $x$ or $y$ value. For q=1 and q=2 a straight line was also used to further mask the data.

The isolation of the parabolas seen in figure 11 was done with different magnetic field strengths per charged state. In figure 12 all the upper and lower bounds of the magnetic field strength are shown as rainbow plots of eq. 20 and eq. 28 to show the approximate kinetic energy of ions in a certain area.

## 4.3 Fitting the data

The mask seen in figure 12a was used to fit eq. 1 and eq. 2 on. The fit, when performed with the same bounds as put on the data, returned different values depending on the initial guess, 0.0204 T and 0.0198 T with costs 0.1751 and 0.1765 respectively. But when values outside of the bounds are allowed, the lowest cost value is 0.1018 for $B$ =0.0232 T. To understand this better, and because the Nelder-Mead fitting method does not calculate the variance or error on the fit since it is a non-derivative fitting method, figure 13 shows the cost values for 2000 evenly spaced magnetic field strength values between 0.0175 T and 0.0238 T and figure 14 shows how they compare to the data they were fitted on. Figure 15 shows how they compare to the unmasked data.

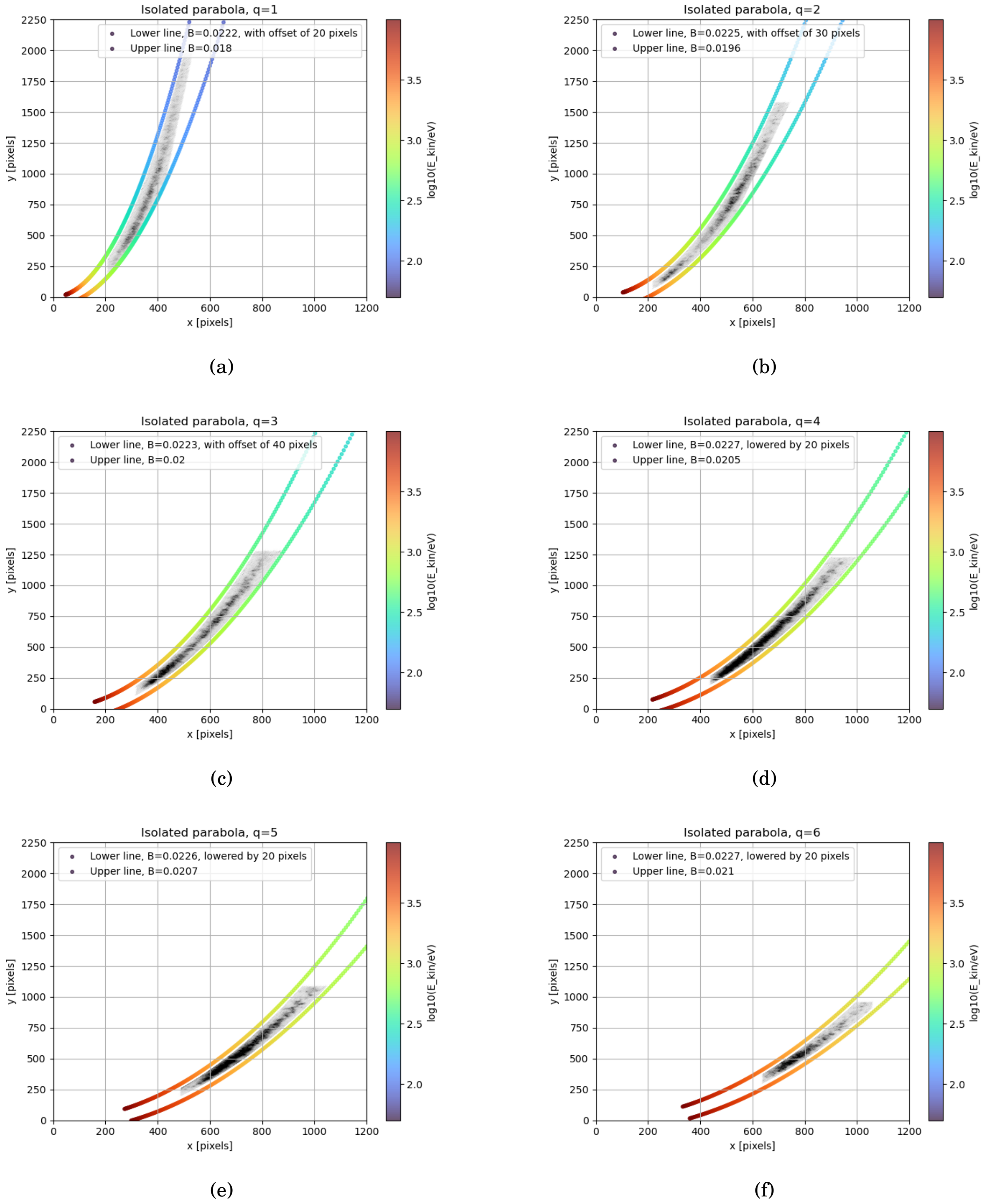


Figure 12: All parabolas from measurement 40 V, 400 mA and 40 mJ visible with their upper and lower bound mask, determined by eq. 20 and eq. 28 and the noted down magnetic field. These are plotted as rainbow plots so approximating the kinetic energy for certain areas is possible. The lower bound is plotted 20 pixels lower, except for $q = 2$ in figure 12b and $q = 3$ in figure 12c.

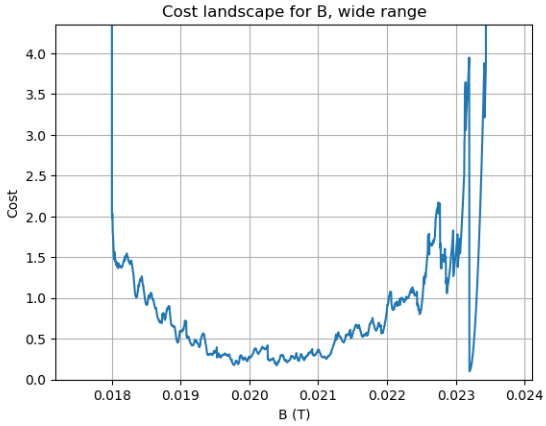


Figure 13: The cost values from the fit on figure 12a plotted against their magnetic field strength. The lowest cost is outside of the bounds and therefore will not be used in further analysis.

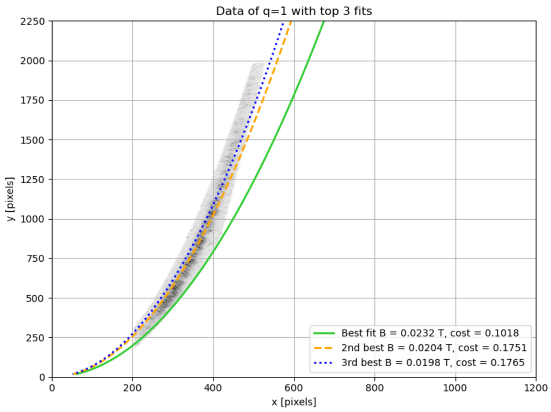


Figure 14: Top three fits on the data of q=1 in figure 12a. The fits are done with eq. 1 and eq. 2 using the Nelder-Mead fitting method. See figure 13 for how these magnetic field values were decided.

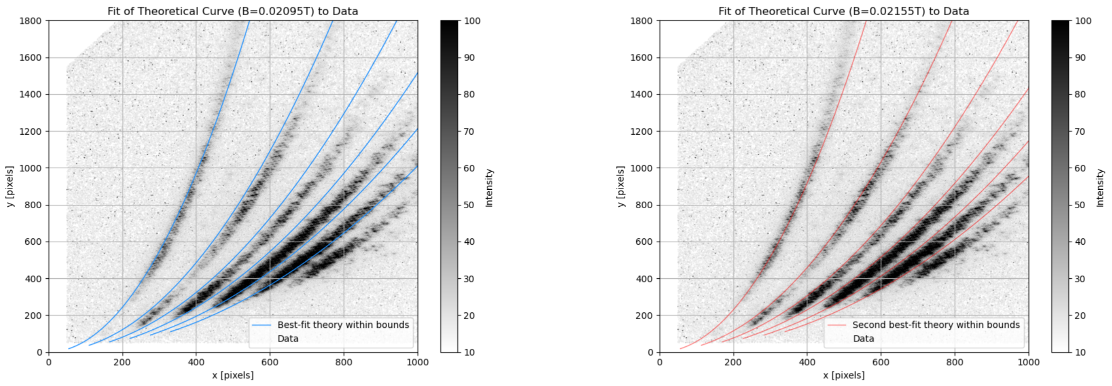


(a) (b)

Figure 15: The two best fits of figure 12a within the given bounds plotted on the unmasked data. The fits overlap mostly with the $q = 1$ data, with 15a being better while 15b is better for higher ionization states. But both fits are not satisfactory for ionization states higher then 2+.The fitted lines for $q = 6$ are for both figures better fitted for the $q = 5$ parabola.

## 4.4 Energy spectrum

The preliminary results of the energy spectrum of all visible charged states constructed as described by section 3.2.3 is shown in figure 16. The x-axis shows the logarithmically scaled kinetic energy, where the bins of the plots are evenly spaced apart. It is preliminary because the energy is calculated with the upper bound magnetic field shown in figure 11, and the background is not fully filtered out, hence the strict masks.

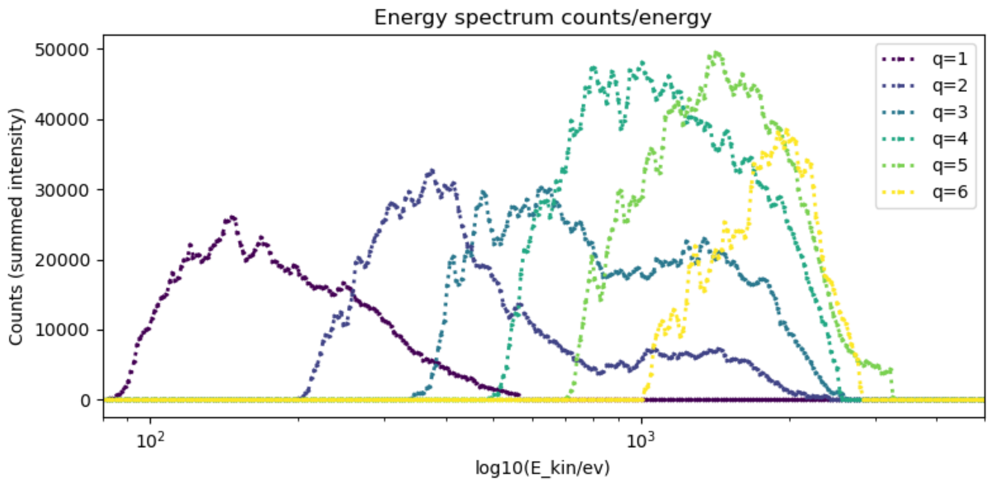


Figure 16: Caption

# 5 Discussion

In this section the results will be discussed in the same order as used in the method and results. Starting with the rotation and determining the origin, followed by the masking and fitting the data and ending with the energy spectrum. The main focus will be on the fitting and why it does not overlap for higher energy states and how the energy spectrum should be interpreted.

## 5.1 Rotating the image

The linear fit performed on the electric fields averaged over one image has a fairly small error and has an acceptable overlap with the data, as can be seen in figure 7. Still, the error of the linear fit on only the magnetic-field data is smaller, confirming that the overlap in electric-field measurements and stricter mask were needed to make a more accurate fit.

The angle between the fitted line gives a promising $89.80\,^\circ$. This difference in angle between the expected $90\,^\circ$ can be attributed to a angle difference in the setup of the coil and capacitor plates. That has not been investigated further. The error due to this difference with $90\,^\circ$ on the $x$ coordinate is negligible: $\cos(89.8) \approx 0.349\%$. Additionally the intersection between the lines give an accurate point of origin. When rotating the electric field data by $(62.654 \pm 0.030)\circ$ and putting the intersection at $(0,0)$, the electric field data overlaps well with the y-axis. Thus this transformation can be applied to other measurements for their analysis.

## 5.2 Implications of the masks

Figure 11 shows the measurement with 40 V and 400 mA on the capacitors and coil rotated and transposed like described in the last paragraph. Additionally it shows the masks put on the data. These masks and the use of the data described in section 3.2.3 have some aspects and implications that warrant discussion and possible improvements.

First, the current data used for analysis only has the zero-field measurement subtracted, and not other background coming from scattered ions. This means that there is signal where there should not be. What makes this more difficult, is that the amount of background signal is not homogeneous. For example, in figure 10b the background between the parabolas, especially between $q = 2$ and $q = 3$ is less than the background above $y = 1500$ and $x = 800$. So when subtracting the background from one part of the plot off of the other plot, the signal can become negative, which is physically impossible. Due to the scope of this thesis, the discussions about how to filter out background were only partially had and filters were not applied. This means that the fits and counts in the energy spectrum are made with this background. To still keep the analysis as accurate as possible strict masks were put onto the data, bringing us to the second implication of the masks performed.

The masks put on the data have a minimum $x$ and maximum $y$ component, meaning the signal we might be interested in gets cut off, especially for the lower energy ions. When comparing it to figure 12, you may be able to faintly see some signal after the mask. The signal-to-noise ratio is considered too small here for accurate analysis. Thus during the analysis and for the results, it is kept in mind that there may be some loss of signal.

Another way some signal might be lost is when the ions with an extremely high kinetic energy hit the beam-stopper. Looking at figure 10b, we can say with confidence that this does not happen, with a possible exception for 2+ ions. The extent of this loss is unknown but can be measured with a measurement when the beam-stopper is taken out, as long as it does not damage the MCP, or by doing the measurement with a Faraday cup with RFA.

The final aspect of the mask is that when the parabola's in the data are close together, the masks of two neighboring parabolas will overlap, as shown in figure 11. While this only happens in parts where mostly the background overlaps, see figure 12, it does need to be taken into account in further analysis of these parabolas.

### 5.3 Fitting

Figure 13 and 14 show a peculiar result on the fit performed on $q = 1$ as shown in figure 12a. The lowest cost fit, which is outside of the bounds of the mask, will be disregarded because it does not overlap well with the data. The reason why this is the lowest cost fit is unknown. The other two fits, look better but still not quite satisfactory. While fit 2 overlaps well with the most intens part of the parabola, the beginning and last part of the parabola seems off. The beginning needs to be less steep while at lower energies the ions get deflected more than is possible for a parabola.

The possibility that this deviation is due to an inaccurate point of origin was also looked at, but no better fits were found. That is, as explained before, because the beginning needs to be less steep while the higher parts need to be more steep. So from figure 14 we can say that the signal is not a parabola. That can also be seen when we overlap these fits on the unmasked data, as done in figure 15. With both fits, the fitted line overlaps best at $q = 2$, but start to go off the signal with higher ionization states.

This additionally cannot be due to using the wrong combination of electric and magnetic field strengths. When combining eq. 1 and eq. 2, a wrong electric field can be offset by a different magnetic field strength, because $y \propto \frac{E}{B^2}x^2$. Meaning the fit would return the same line. thus concluding, the data does not compare to the theory. This was also seen in figure 3.2 and 3.5 in Tinge's report [4], as well as experiments done in October of 2024 by Laurens van Buuren. Figure 17 shows a side-by-side with his data and best fit over $q = 1$. The difference in magnetic field, added onto the worsened overlap of the fit would suggest the coil or something different around the magnetic field has changed in between these measurements. After these results van Buuren measured the magnetic field along the paths of the ions to be roughly 0.02 T, further supporting the indication that something about the magnetic field has changed.

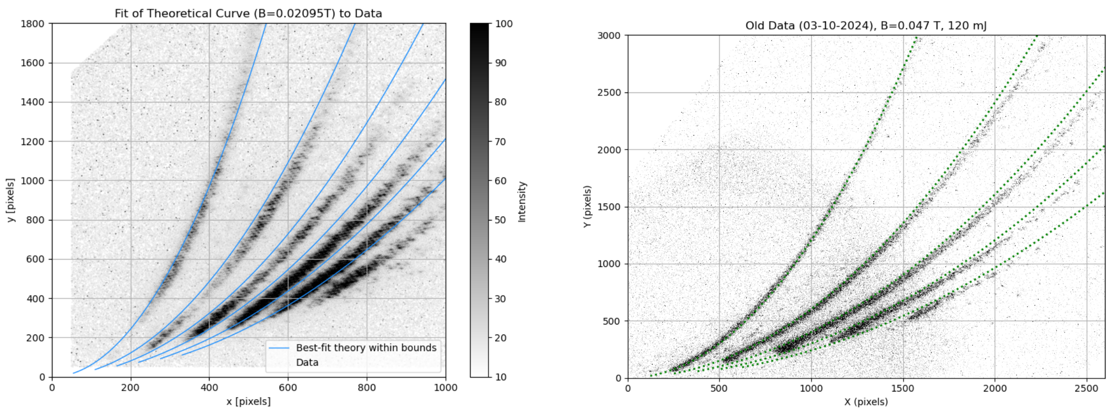


(a) (b)

Figure 17: Old data and fit from Laurens van Buuren made in October 2024 compared to newer data and best fit. Both fits are not completely satisfactory for higher ionization states, though van Buuren's fit is significantly better. Both measurements taken on the same setup with the method being the same, except that the newer data is made after a realignment of the apertures and the target and the laser intensity is 120 mJ, instead of 40 mJ. With both measurements the voltage on the capacitors is 40 V and the current on the coil 400 mV. Newer data looks more blurry because of the plotting method in the code (scatter v.s. pcolormesh with matplotlib.pyplot).

The common limitation of Tinge's equations, van Buuren's fit, and the method and theory used here is that the electric field is assumed to be homogeneous. A non-homogeneous electric field, that affects slower ions more than faster ions, would explain why the fit overlaps only with the medium speed ions and not the slower or faster ones. That would also explain why the parabolas from higher ionization states are less deflected then expected, since they also go faster. Tinge's report shows, using SIMION simulations, found that the electric field is not homogeneous and does have a bigger impact than the homogeneous field theory suggests [4]. So the conclusion that the electric field is inhomogeneous is supported by previous research using the same setup.

## 5.4 Preliminary count energy spectrum

Figure 16 shows the preliminary results of the energy spectrum. In the figure, bunching of higher ionized ions at higher kinetic energies can be seen as well as the +1 ions starting at significantly lower kinetic energies. This is in line with results from Poirier et al. using a Faraday Cup with a RFA [2].

The energy spectrum result is preliminary because in addition to the limitations on the masks and theory described earlier, the method has some limitations. The main limitation is that figure 16 is calculated only with the bins on the upper bound of the mask. It would be more accurate to have a line going through the middle of the parabola on which the energy spectrum is calculated.

Additionally, an error on the counts is missing. The error on the energy spectrum consists of two parts, the mismatch between theory and results and the amount of background. The mismatch between theory and results generally impacts the x-axis, not the number of counts. This impact of this mismatch is unknown, but can be found out by using formulas meant for inhomogeneous fields or can be negated by changing the setup to make the electric field more homogeneous, like adding a grid. For the interpretation of figure 16, the x-axis should not be assumed to be correct, but this does not significantly impact the shape of the figure. The background does. If the background is assumed to be roughly homogeneous, the lower energies will have higher counts. This is due to the mask broadening at lower energies compared to the higher energies and because of how the bins are set up on the upper bound. The kinetic energy increases logarithmically. This means that higher energies have more bins plotted on the image compared to lower energies. This can be seen in figures 12c and 12d, where the individual bins are visible at the lower energies. The consequence is that in figure 16 the signal at lower energies is higher because of the background signal.

Lastly, figure 16 should not be interpreted as a dQ/dE graph. In this setup there is a significant difference between the amount of counts and the amount of counted ions. The counts used are the counts on the pixels in the picture taken by the camera. These counts range from 0 to 255. For the figure to be made into a dQ/dE graph, it needs to be known how many ions cause a certain amount of pixel counts.

## 5.5 Outlook

To improve the accuracy of the energy spectrum, a couple of things need to be done. Starting with finding a way to get rid of the background noise. This can be done by subtracting the average background noise and concluding there are no ions when the signal is negative, or by another method. This needs to be further analyzed and researched.

Another improvement for future measurements is placing a wire mesh on the capacitors, making the field more homogeneous. This mesh, like a Faraday cage, would limit the components of the electric field outside of $L_E$ generated by the capacitors. The downside of this mesh would be the increased background signal, coming from ions that collide and scatter on this mesh. The current setup appears to have a high enough signal-to-noise ratio for this to work, but this would need to be tested.

Additionally, the fit in figure 8 can be done with weights put on the intensity. Although the fits returned a point of origin with a small error, performing a weighted fit would improve the accuracy of the point of origin and angle with which data needs to be rotated.

Furthermore, the Thomson Parabola can be calibrated by directing an ion beam, with a known kinetic energy, into the setup and comparing the expected deflection with the measured deflection. This can be done using the ion beam setup located at the Zernike low energy ion facility in Groningen, described in [6].

Finally, to transform the current energy spectrum into a $dQ/dE$ spectrum, the impact of higher ionized ions, as well as high velocity ions, on the signal given by the MCP needs to be known and accounted for. Poiriers results would suggest, when comparing with our results, that the MCP returns a higher intensity with higher ionization and velocity ions, meaning in our the intensity in figure 16 for higher ionized ions would need to be lowered. [2].

## 6 Conclusion

In the current setup the energy spectrum of ions coming from an LPP can be measured in a single shot using eq. 1 and eq. 2, but the accuracy is limited. This energy spectrum, figure 16, shows bunching of higher ionized ions at high kinetic energies as well as the +1 ions starting at an significantly lower kinetic energy then the other ionization states.

Eq 1 and 2 were compared with equations that did not have any assumptions in their derivation, apart from homogeneous fields, eq. 20 and eq. 28. This comparison showed no significant differences within the expected range of deviation. The main finding is that the theory does not overlap with experimental data. The ions are affected differently than the expected parabolas, presumably because the electric field, that in theory was homogeneous, has inhomogeneous regions. The accuracy of both the fit and energy spectrum can be further improved by improving the filtering of the background and accounting for its associated error. Lastly, the energy spectrum can be made into a $dQ/dE$ spectrum when accounting for the rate of intensity per ion per ionization state.

# References


[1] Katie Tarasov. *Exclusive look at the creation of high na, ASML's new* $400 millionchipmakingColossus$. May 2025. URL: `https://www.cnbc.com/2025/05/22/exclusive-look-at-high-na-asmls-new-400-million-chipmaking-colossus.html`.

[2] L. Poirier et al. "Energy- and charge-state-resolved spectrometry of tin laser-produced plasma using a retarding field energy analyzer". In: *Applied Physics B* 128.7 (2022), p. 135. ISSN: 1432-0649. DOI: `10.1007/s00340-022-07844-5`. URL: `https://doi.org/10.1007/s00340-022-07844-5`.

[3] D.C. Carroll et al. "A modified Thomson Parabola Spectrometer for high resolution multi-mev ion measurements—application to laser-driven ion acceleration". In: *Nuclear Instruments and Methods in Physics Research Section A: Accelerators, Spectrometers, Detectors and Associated Equipment* 620.1 (Aug. 2010), pp. 23–27. DOI: `10.1016/j.nima.2010.01.054`.

[4] L. Tinge L. Buuren. *Design and characterisation of a Thomson parabola for determination of charge and energy distribution of tin plasmas*.

[5] Pauli Virtanen et al. "SciPy 1.0: Fundamental Algorithms for Scientific Computing in Python". In: *Nature Methods* 17 (2020), pp. 261–272. DOI: `10.1038/s41592-019-0686-2`.

[6] S. Rai et al. "Charge exchange in collisions of 1–100-keV $Sn^{3+}$ ions with $H_2$ and $D_2$". In: *Phys. Rev. A* 106 (1 July 2022), p. 012804. DOI: `10.1103/PhysRevA.106.012804`. URL: `https://link.aps.org/doi/10.1103/PhysRevA.106.012804`.